Preparation and characterization of magnetite modified nanoparticles with *p*-benzoquinone-ethylenediamine for adsorption of humic acid from aqueous solution

S. Beiki[a], E. Moniri[b],*, A.H. Hassani[c], H.A. Panahi[d]

[a]*Department of Natural Resources and Environment, Tehran Science and Research Branch, Islamic Azad University, Tehran, Iran, Tel. +98-9194324039; email: Somayeh.beiki@srbiau.ac.ir*
[b]*Department of Chemistry, Varamin (Pishva) Branch, Islamic Azad University, Varamin, Iran, Tel. +98-9125011003; email: moniri30003000@yahoo.com*
[c]*Tehran Science and Research Branch, Department of Natural Resources and Environment, Islamic Azad University, Tehran, Iran, Tel. +98-9121039899; email: ahhassani@srbiau.ac.ir*
[d]*Department of Chemistry, Central Tehran Branch, Islamic Azad University, Tehran, Iran, Tel. +98-9126026038; email: H.ahmadpanahi@iauctb.ac.ir*

a b s t r a c t

In this report, a novel modified magnetite nanoparticles/*p*-benzoquinone (BQ)-ethylenediamine (E) (MMNP/BQ-E) composite was introduced as a linear chain polymer. The adsorbent was prepared via grafting chemical method, in which $Fe_3O_4@SiO_2$ was the core and five generations modified by BQ and E were coated on the surface of the $Fe_3O_4@SiO_2$ as shells. The MMNP/BQ-E was used for removal of humic acid (HA) from aqueous solutions using batch adsorption technique. Optimal adsorption conditions including pH, contact time, initial HA concentration, and adsorbent dosage were investigated. The characterization of MMNP/BQ-E was performed using X-ray diffraction (XRD), X-ray photoelectron spectroscopy (XPS), Fourier transform infrared spectroscopy (FTIR), scanning electron microscopy, energy dispersive X-ray analysis (EDX), Brunauer–Emmett–Teller (BET) analysis, and Barrett–Joyner–Halenda. The specific surface area of MMNP/BQ-E was found to be 58.34 m^2 g^{-1}. The modification was confirmed by FTIR, XRD, and XPS analysis. According the XRD analysis, the average diameter of MMNP/BQ-E was obtained as about 11.26 nm. The Langmuir, Freundlich, Temkin, Redlich–Peterson, and Dubinin–Radushkevich (D–R) adsorption isotherm models were used to obtain the maximum adsorption strength. The results indicated that the adsorption isotherms were better fitted by the Langmuir model, where pseudo-second-order better explained the adsorption kinetics of HA onto MMNP/BQ-E with regression coefficient (R^2) of 99%. The adsorption strength of MMNP/BQ-E was found as large as 20.36 mg HA g^{-1}, leading to 99% removal at 25°C. Further, the investigated thermodynamic parameters indicated the spontaneity of the adsorption process in nature.

Keywords: Modified magnetite nanoparticles; *p*-Benzoquinone-ethylenediamine; Humic acid; Adsorption

1. Introduction

In today's world, clean water is not accessible to most people. Therefore, safe drinking water is not easily available which is of great importance for our life [1]. One of the reasons for water-related diseases is pathogens which lead to infection or worm diseases and diarrhea [2]. Other common pollutants of water are organic residues which originate from major industries, such as pulp, textile, and steel

* Corresponding author.

refineries [2]. They are less dangerous than pathogens, but they cause color-, taste-, and odor-related problems [3]. One of the natural causes of water contamination is humic substances that arise out of biodegradation of plants [4]. Humic acid produces undesirable color, taste, and odor, though it is not directly toxic [5]. It also reacts with chlorine during disinfections of drinking water [6] thereby producing carcinogenic disinfection by-products [3].

The humic acid concentration of natural waters is below 10–15 mg L^{-1} [7]. There are two general methods for water treatment and removing humic acid from drinking water: centralized and decentralized methods. Centralized methods include coagulation, filtration, sedimentation, disinfection, [8] but each of them is used for a specific situation. As an instance, in densely populated areas, the centralized water treatment is employed while it is infeasible for developing countries as they are far away and have higher costs [1]. It is also infeasible in rural areas due to the use of untreated private groundwater supplies [9]. Coagulation which uses alum is a traditional method which is costly and produces sludge [4]. On the other hand, decentralized methods include membrane separation, filters, adsorption, boiling, and solar disinfection [1,4]. These methods produce clean drinking water from existing water sources such as rain and river water [1]. These methods are useful for disaster-stricken areas where people are at risk of diseases caused by sanitation and water supply problems after a disaster. Membrane separation as one of the decentralized methods will restrict the removal capacity of humic acid [4]. For example, Norfazliana et al. [10] have investigated the performance evaluations of alumina hollow fiber membrane incorporated with UiO-66 particles for HA removal. The most favorable removal method which is simple and cost-effective is the adsorption of humic acid. Derakhshani and Naghizadeh [11] have optimized HA removal by adsorption onto bentonite and montmorillonite nanoparticles. In a similar study, Salla et al. [12] have considered Mn_2O_3 and α-Al_2O_3 nanoparticles as adsorbents for removal of HA from aqueous solution or Ye et al. [13] have studied on preparation of TiO_2/graphene composite with appropriate *N*-doping ratio for HA removal.

At present, because of the large specific surface area of magnetic metal oxides (such as Fe_3O_4) and due to their small internal diffusion resistance, they have become more popular as vigorous dye adsorbents [14]. Pollutants from aqueous solutions can be absorbed by magnetic nanoparticles and afterward they can be separated from water with a minimal magnetic process [15]. Modification of the Fe_3O_4 nanoparticles has been proposed by many researchers in order to provide a better surface specificity for removing different dyes from aqueous solutions. Lu et al. [16] investigated montmorillonite/Fe_3O_4/HA nanocomposites for simultaneous removal of Cr(VI) and aniline. The mentioned modification can be done by various chemicals such as polyacrylic acid [17], humic acid [18], carboxymethyl-cyclodextrin [19], yeast [20], graphene oxide [21,22], zinc oxide [23], and multi-wall carbon nanotube [24]. The surface of nanoparticles can be altered by a polymer to enrich the distribution and stability of adsorbents in aqueous solutions [25].

In this study, a novel modified magnetite nanoparticle (MMNP) is developed by grafting amino groups (benzoquinone-ethylenediamine) to coat the surfaces of Fe_3O_4@SiO_2 by grafting method. The MMNP/B-E with core-shell structure is polymerized for the removal of HA from aqueous solutions. As a core, the structure of MMNP/B-E is introduced by Fe_3O_4@SiO_2 after which as a shell, five generations of chain polymer are introduced. The aim of this study is to provide an executable method for the removal of HA from water to investigate the adsorption characteristics and mechanism of HA using novel nanoparticles as an effective absorbent. Furthermore, regeneration properties of the MMNP/BQ-E were surveyed. The effects of various experimental conditions such as sorbent weight, pH, contact time, initial concentration of HA, on the MMNP/B-E are investigated using batch experiments. After the adsorption process, the separation of the nanoparticle is performed by an external magnet.

2. Experimental

2.1. Materials and methods

All materials were of commercial reagent grade and used as received without further purification. The reagents used for the preparation of Fe_3O_4 nanoparticles and synthesis MMNP/BQ-E were purchased from Merck (Germany). Deionized water was used in all experiments. HA was purchased from Sigma-Aldrich (USA) Chemical. HA stock solution was provided by dissolving 100 mg of HA powder in 1 L of distilled water where the solution was mixed utilizing a magnetic stirrer. The solutions for all adsorption tests were provided by enhancing the HA to stock solution for achieving the preferred HA concentrations.

2.2. Synthesis of Fe_3O_4@SiO_2

Step 1: The magnetite nanoparticles were synthesized via co-precipitation method. We prepared a solution containing 0.99 g of $FeCl_2 \cdot 4H_2O$, 3.25 g $FeCl_3 \cdot 6H_2O$ and 70 mL of distilled water. While the solution was stirred, 15 mL of ammonia solution (25%) was added until the pH was fixed within 11–12. Then, the solution was stirred under nitrogen reflux at 80°C for 2 h. For Fe_3O_4@SiO_2 synthesis, 80 mL of ethanol and 40 mL of tetraethylorthosilicate (TEOS) were added to the Fe_3O_4 solution and stirred for 24 h at 25°C. After this time, the Fe_3O_4@SiO_2 was taken up by an external magnet, and washed with distilled water and 30 mL of ethanol, and finally dried at room temperature.

2.3. Amino-functionalized Fe_3O_4@SiO_2

Step 2: (3-Aminopropyl) trimethoxysilane (APTMS) was used as surface functionalization agent for Fe_3O_4@SiO_2 nanoparticles. For this purpose, 5 mL (APTMS), 95 mL dry toluene, and 3 g of Fe_3O_4@SiO_2 nanoparticles were added while the solution was kept under nitrogen reflux for 16 h at 95°C. Thereafter, the resulting nanoparticles were collected by external magnetic stirrer and were left to dry at room temperature.

2.4. Modified Fe_3O_4@SiO_2-APTMS

Step 3: A total of 3 g of the nanoparticles prepared in the previous stage plus 1 g of *p*-benzoquinone ($C_6H_4O_2$) (BQ)

were added to 150 mL ethanol solution. The solution was stirred under nitrogen reflux for 8 h at 50°C. After this time, $Fe_3O_4@SiO_2$-APTMS-BQ was collected by an external magnet, washed with 20 mL of ethanol, and dried at room temperature. The nanoparticles obtained from this stage were called $G_{0.5}$.

Step 4: Here, 30 mL ethylenediamine (E) and 3 g of the previous step nanoparticles were added to 150 mL of the methanol solution. The solution was stirred under nitrogen reflux at 50°C for 8 h. The $Fe_3O_4@SiO_2$-APTMS-BQ-E nanoparticles were washed with 20 mL of methanol and dried at room temperature. This generation was called G_1.

Step 5: To obtain the fifth generation, we repeated steps 3 and 4 four times. After this cycle, the third stage was repeated once again.

Step 6: In the last step, end-groups were linked to the nanoparticles' chain. For this purpose, 10 mL of 4-amino acetanilide as the ligand and 3 g of previous step nanoparticles were dispersed in 150 mL of the ethanol solution. The solution was stirred under nitrogen reflux for 8 h at 40°C. Finally, the magnetite modified nanoparticles/benzoquinone-ethylenediamine (MMNP/BQ-E) were washed with 20 mL of ethanol and then dried at room temperature. The synthesis and modified process of MMNP/BQ-E is displayed in Fig. 1.

2.5. Adsorption and desorption experiments

All the adsorption experiments of HA on MMNP/BQ-E were carried out in batch mode at 25°C. The adsorption experiments were performed at 150 rpm for the specified time via magnetic agitation on an electromotive stirrer (MY3000-6, MEIYUYIQI CO., China). For all experiments, the MMNP/BQ-E was separated from HA solution by an external magnet followed by filtration. Then, the supernatant was analyzed using UV–Visible spectrophotometer (PerkinElmer 3100 Model, Artisan Technology, USA). To investigate the effect of pH on HA removal, the pH measurement was performed within 3–10 with 2 mg of adsorbent at 25°C for 5 min in 20 mg L⁻¹ HA solution. The pH values were adjusted by adding magic buffer (1.438 mL acetic acid, 1.675 mL phosphoric acid and 1.236 g boric acid were dissolved in distilled water up to 500 mL) and NaOH 0.1 M. Then, the pH of solutions was measured by a pH-meter (Aqualytic AL15). In order to investigate the effect of contact time on the adsorption of HA, the HA solution (20 mg L⁻¹) was shaken continuously with 2 mg of the adsorbent within 5–120 min at the optimum pH at 25°C. The recording time started when MMNP/BQ-E nanoparticles were added to the HA solutions. The initial concentration of HA was applied with various initial HA concentrations (0.5–30 mg L⁻¹) at optimized pH = 6 and contact time = 20 min with 2 mg of adsorbent at 25°C. To investigate the effect of the amount of MMNP/BQ-E (0.05–1.5 g) on HA removal, the optimized initial concentration HA (10 mg L⁻¹) at pH = 6 was shaken at 25°C for 20 min. To study the thermodynamic parameters, experiments were carried out at the optimized values at five various temperatures (298, 303, 308, 313, and 318 K).

The adsorption percentage (Ads %) and the rate of HA adsorbed at time t (q_e and q_t mg g⁻¹) were computed by Eqs. (1) and (2):

$$\text{Ads \%} = \frac{C_0 - C_e}{C_0} \times 100 \qquad (1)$$

$$q_e = \frac{C_0 - C_e}{m} \times V; \quad q_t = \frac{C_0 - C_t}{m} \times V \qquad (2)$$

where C_0 is the initial HA concentration (mg L⁻¹), C_e shows the amount of HA present in the solution at equilibrium time t (mg L⁻¹), V denotes the volume of HA concentration (mL), and m is the dry weight of the sample (g).

K_d (mL g⁻¹) reflects the distribution coefficient of adsorption process which is computed from Eq. (3):

$$K_d = \frac{C_0 - C_e}{C_e} \times \frac{V}{m} \qquad (3)$$

In order to estimate the reusability of MMNP/BQ-E adsorbent, the adsorption–desorption cycle was repeated eight times under optimal conditions. In each cycle, 10 mg L⁻¹ of HA solution was mixed with 0.5 g of MMNP/BQ-E adsorbent for 20 min. The MMNP/BQ-E nanoparticles were separated magnetically followed by 0.45 μm filtration. UV–Vis spectrophotometer was used for HA measurement in the solution (first cycle). The resulted sorbent of the first cycle, conducted with 10 mL of 0.01 M NaOH in ethanol solutions for 15 min at 50°C. After the HA desorption, the regenerated adsorbent was magnetically collected for use in the next adsorption–desorption cycle.

2.6. Analytical method HA

Ultraviolet (UV) adsorption is a fast and easy way to measure the amount of HA in the sample. UV–Vis spectroscopy measurement carried out in the range of 200–400 nm and HA has a maximum absorbency at a wavelength of 254 nm (λ_{max}). After the adsorption process, the adsorbent was collected by an external magnet followed by 0.45 nm filtration. Residual concentration of the HA (supernatant) was measured at 254 wavelengths. The UV–Vis spectrophotometer was calibrated using the Milli-Q water as a blank.

2.7. Ionic strength on the HA adsorption

NaCl solution (0.01–1 mol L⁻¹) used to investigate the ionic strength effect on the HA adsorption onto the MMNP/BQ-E nanoparticles. By means of batch experiments, each tube contained 10 mg L⁻¹ HA, 0.2 g L⁻¹ adsorbent and NaCl solutions with different ionic strengths (0.01–1 mol L⁻¹) brought to pH 7 and agitated for 12.0 h at 25°C. After filtration by 0.45 μm membrane, the remaining HA concentration (supernatant) was measured using UV–Vis spectrophotometer and results expressed as adsorption capacity percentage.

3. Results and discussion

3.1. Characterization of the synthesized MMNP/BQ-E

The crystalline structure and the composition of the MMNP/BQ-E were characterized by X-ray diffraction (XRD) (Philips PAN Analytical X'pert Pro) and X-ray fluorescence (XRF) applying a scanning speed of 0.015/Second and Cu Kα
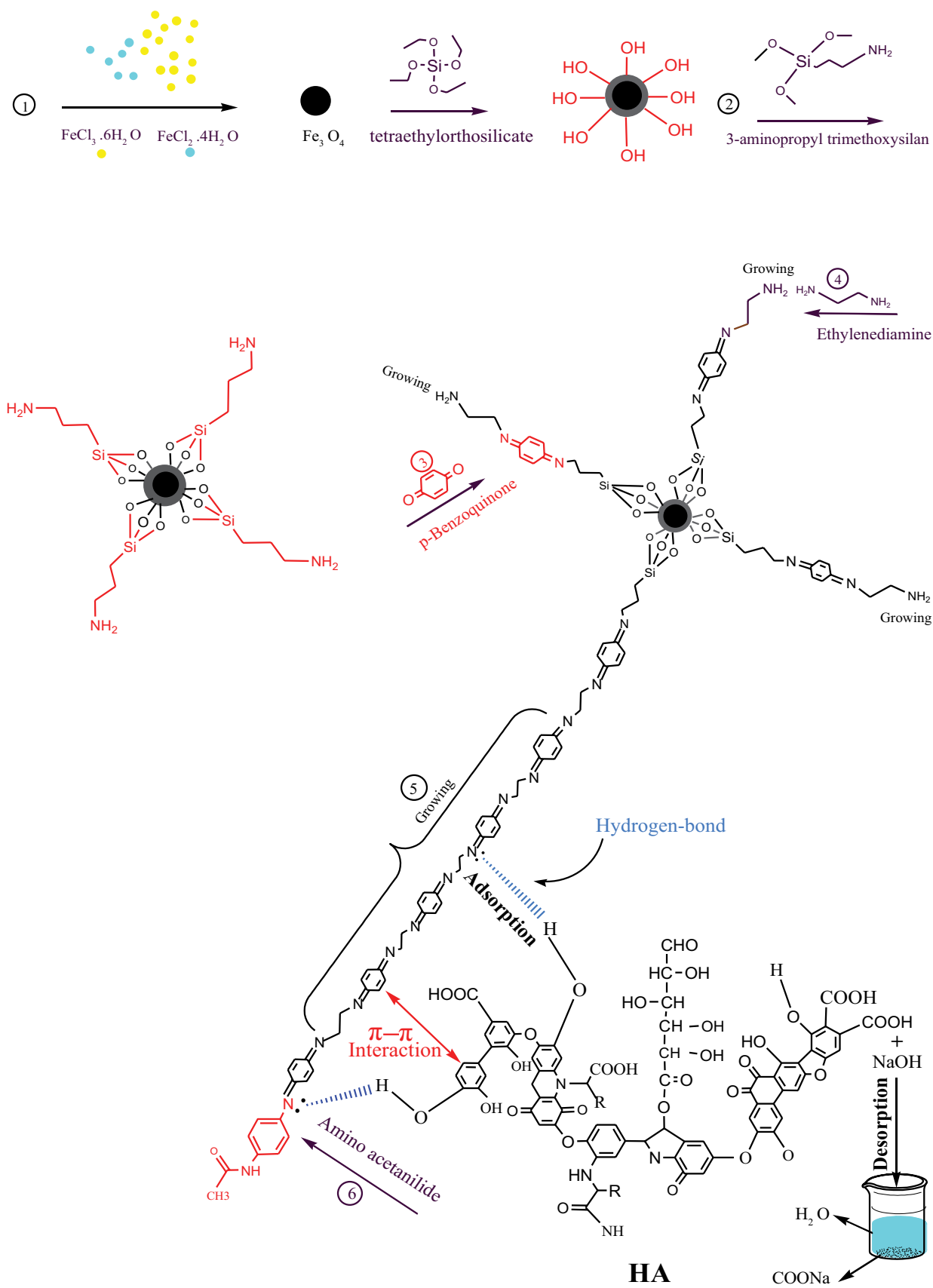
Fig. 1. Synthesis and modifying process of MMNP/BQ-E.

line radiation (λ = 1.54056 Å) with voltage and current of 40 kV and 40 mA, respectively. X-ray photoelectron spectroscopy (XPS) tests were performed on a Thermo Scientific K-Alpha 1063 (Thermo, USA). The morphology of MMNP/BQ-E was characterized by scanning electron microscopy (SEM; Cambridge S-360). To confirm loading of modification onto magnetite particles, we used energy dispersive X-ray analysis (EDX). The Brunauer–Emmett–Teller (BET) specific surface area analysis was determined using Quantachrome NOVA 2200e system (Austria), and the pore size and pore volume were calculated using the Barrett–Joyner–Halenda (BJH). The morphology and size of the resulted MMNP/BQ-E were characterized by transmission electron microscopy (TEM, Zeiss-EM10C-100 kV, Germany). In order to assess the quality of the adsorbing chemical structure, we used Fourier transform infrared spectroscopy (FTIR) spectrophotometer (Vector 22 Bruker Company, USA). The UV–Visible spectroscopy (UV–Vis) with λ = 254 nm was employed to determine HA concentration by UV1KON-BIO-TEK Kontron Company, Germany.

3.1.1. XRD study

The XRD pattern of MMNP/BQ-E is presented in Fig. 2. The results indicate generic deflection peaks of 2θ at 30.69°, 35.3°, 43.5°, 53.3°, 57.7°, and 62.2° (JCPDS card 19-0629) [26]

confirming that the crystal magnetite has been distributed all over the surface of the MMNP/BQ-E. Therefore, no change was made on the main composition during the chemical modification. In addition, peaks were observed at 12.98° and 16.6°, which could be attributed to modification on the surface of Fe_3O_4. The averaged crystal diameter from the peaks was obtained via the Scherrer equation (Eq. (4)) [19]:

$$D = K\lambda\beta\cos(\theta) \tag{4}$$

where D is the diameter of the particle, λ denotes the X-ray wavelength, β is the full width at half maximum of the diffraction line, θ shows the diffraction angle, and K is a constant equal to 0.89. According the Scherrer equation, the average diameter of MMNP/BQ-E was obtained as about 11.26 nm.

The elemental composition of the MMNP/BQ-E was determined by XRF spectrometer. The XRF results of the MMNP/BQ-E presented the chemical composition (expressed as the metal oxide content, % w:w) which was controlled by Fe_3O_4 (14.04%) and SiO_2 (73.11%) ratio, respectively.

3.1.2. FTIR study

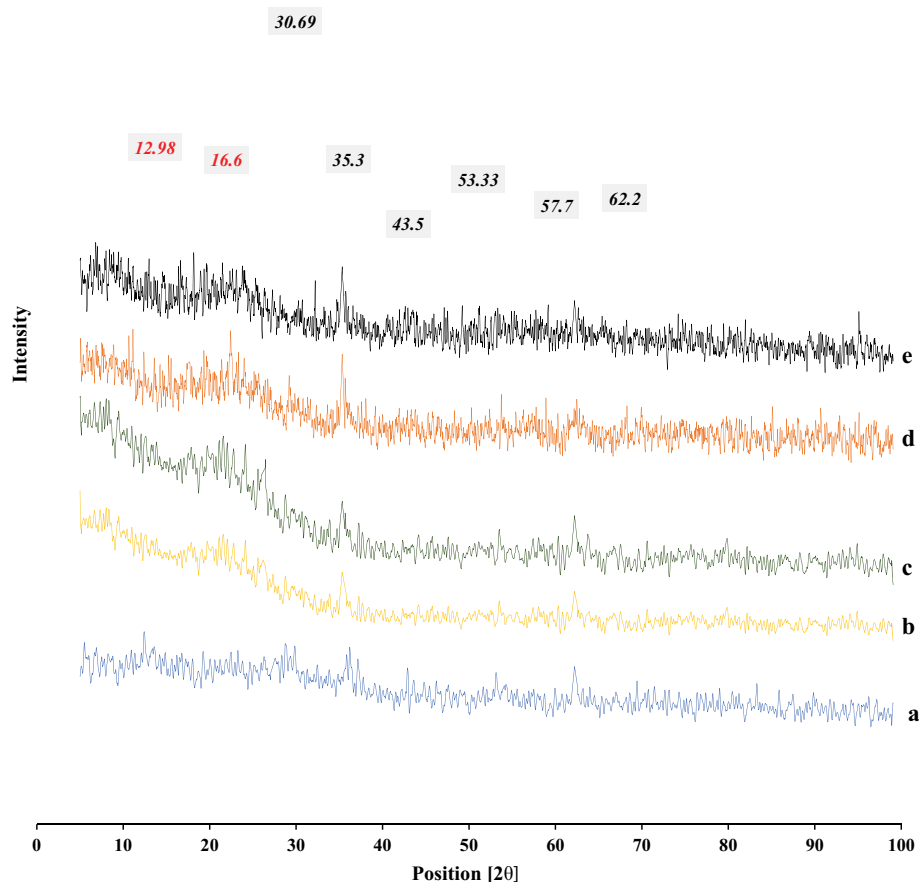The FTIR of MMNP/BQ-E is illustrated in Fig. 3. The FTIR spectra of $Fe_3O_4@SiO_2$ shown in Fig. 3a have a broad

Fig. 2. XRD pattern: (a) $Fe_3O_4@SiO_2$, (b) $Fe_3O_4@SiO_2$-APTMS, (c) $Fe_3O_4@SiO_2$-APTMS-BQ, (d) $Fe_3O_4@SiO_2$-APTMS-BQ-E and (e) MMNP/BQ-E.
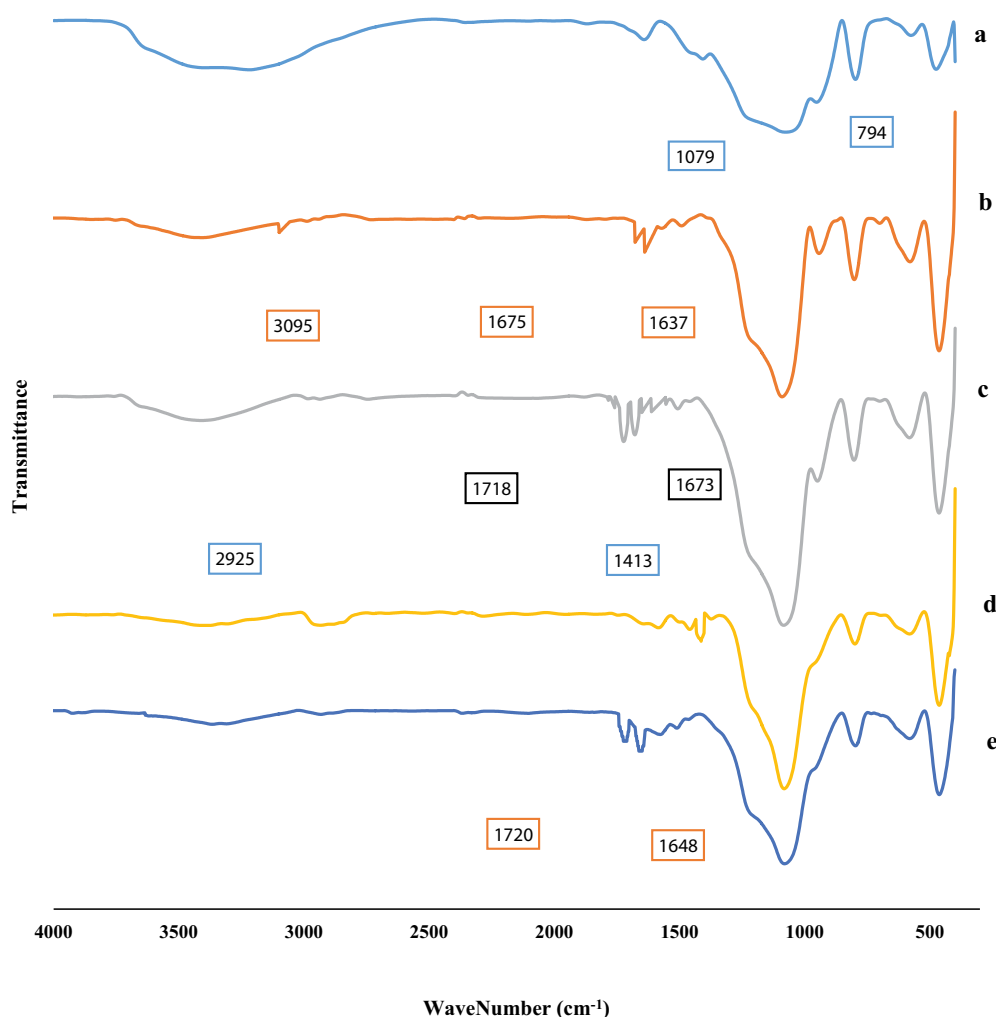
Fig. 3. FTIR spectra: (a) $Fe_3O_4@SiO_2$, (b) $Fe_3O_4@SiO_2$-APTMS, (c) $Fe_3O_4@SiO_2$-APTMS-BQ, (d) $Fe_3O_4@SiO_2$-APTMS-BQ-E and (e) MMNP/BQ-E.

band at 1,079 cm⁻¹ which is related to Si–O [27]. Also, another broad band rising within the range of 3,000–3,600 cm⁻¹ is attributed to stretching vibrations of O–H bonds of TEOS. The FTIR spectrum of the magnetite (Fe_3O_4) at wavenumber of 794 cm⁻¹ which is considered to be associated with Fe–O band [28–30] confirms the spinel type structure of Fe_3O_4. Fig. 3b reveals the band at 1,675 which is related to the NH bending vibration, while another stretching vibration NH at 3,095 cm⁻¹ was observed attributed to APTMS [31]. Also, the next peak at 1,637 cm⁻¹ is related to OH [30,32]. Fig. 2c shows a strong special peak at the wavelength of 1,718 cm⁻¹ corresponding to the C=O bending vibration of *p*-benzoquinone [32,33], while another broad band at 1,673 cm⁻¹ is attributed to bending vibration of C=N. The bending vibration band at 1,413 cm⁻¹ corresponds to the CH_2 which is related to eth-ylenediamine, and next peak at 2,925 cm⁻¹ is attributed to the aliphatic CH (Fig. 3d). Two strong bending vibration bands at 1,648 and 1,720 cm⁻¹ are attributed to NH_2 and C=O, respectively (Fig. 3e), showing a ligand. Overall, all of the wavelengths confirm the modification performed onto the surface of $Fe_3O_4@SiO_2$ nanoparticles.

3.1.3. SEM–EDS study

The surface morphologies of MMNP/BQ-E were charac-terized by SEM as shown with two different scales of 1 μm and 200 nm in Fig. 4. The SEM image exhibits an almost spherical structure and a rugged surface shape with a rough and irregular morphology. The MMNP/BQ-E was analyzed also by EDS, which suggested the formation of the compo-nents of MMNP/BQ-E. The percentages for Fe (8.51%) and Si (15.73%) confirmed that the magnetite has been based the absorbent and covered by silica. Also, the percent-ages of O (30.33%), N (17.28%), and C (28.15%) showed that an organic part has been linked with Fe_3O_4 revealing that the adsorbent structure was well synthesized and the polymerization process of MMNP/BQ-E was performed successfully [26]. Among 1,800 nanoparticles, the approxi-mate size of the nanoparticle image is about 39.12 nm.

3.1.4. TEM study

The TEM image of MMNP/BQ-E shown in Fig. 5, which that indicates the MMNP/BQ-E, is shaped and uniform in
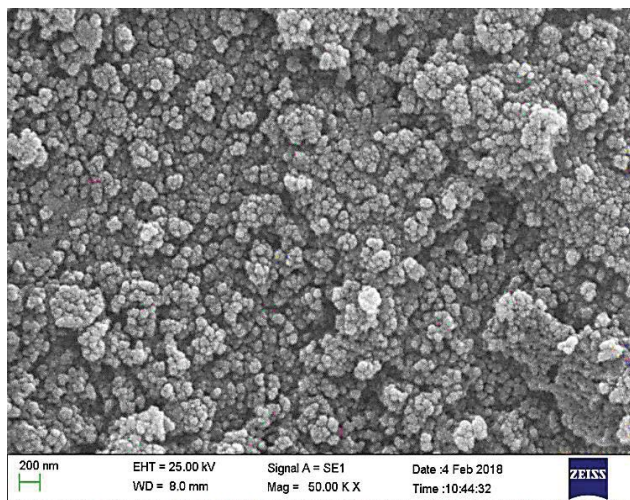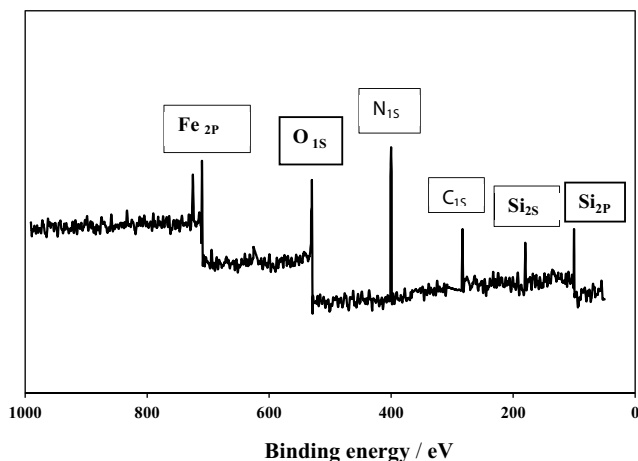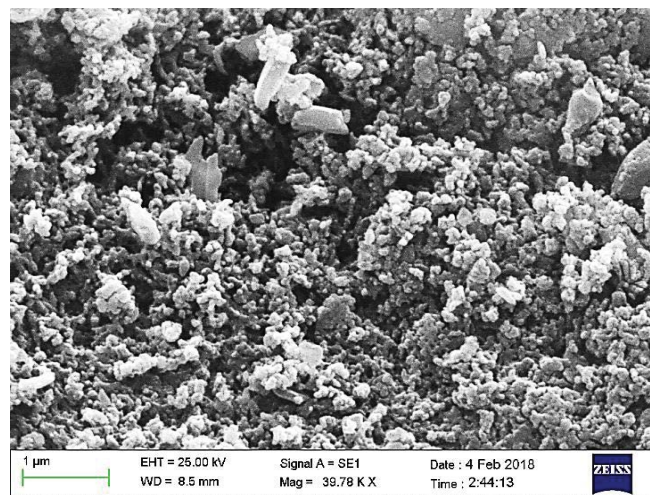
Fig. 4. SEM image of MMNP/BQ-E.

Fig. 5. Full range XPS spectra of MMNP/BQ-E.

size. MMNP/BQ-E has core-shell structure and the silica layers were coated onto Fe_3O_4 with a smooth surface. The TEM image of MMNP/BQ-E existing explicit core-shell structure, in which the Fe_3O_4 core is apparent as a dark zone coated a brighter shell.

3.1.5. XPS analysis

The MMNP/BQ-E is further examined by X-ray photo-electron spectra. Their spectra are shown in Fig. 6 corresponding to the binding energies of Fe_{1S}, Fe_{2P}, and O_{1S} at 709, 722, and 530 eV, respectively. These are consistent with the reported values of Fe_3O_4 in the literature [34] and the XPS results prove the composition of the adsorbent. In accordance with FTIR and XRF results discussed earlier, the binding energy of 400 eV confirms the presence of the great amount of N_2 in the surface of the adsorbent. The OH groups of the HA could hydrogen-bond with amine groups on the surface of adsorbent which is the most effective adsorption mechanism on the MMNP/BQ-E. As shown in Fig. 6, the binding energies of C_{1S} spectrum attributed to *p*-benzoquinone at 283 eV.
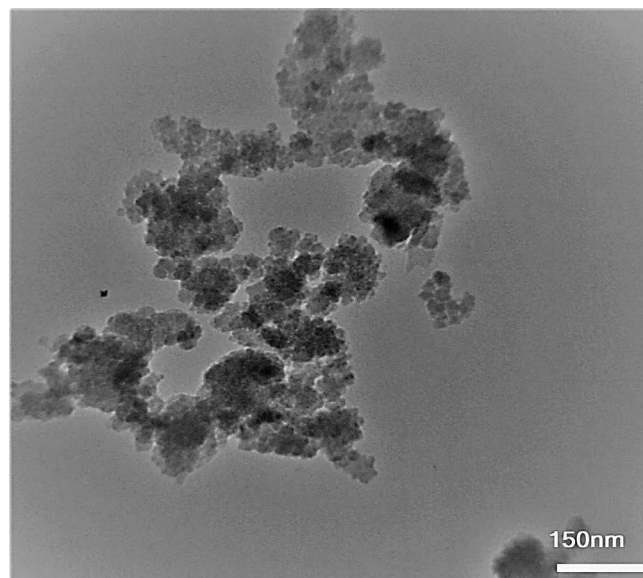

Fig. 6. TEM image of MMNP/BQ-E.

3.1.6. N_2 adsorption–desorption

N_2 adsorption–desorption analysis was used to evaluate the porous nature of synthesized nanoparticles. The BET analysis showed that the surface area of MMNP/BQ-E was 58.34 $m^2\,g^{-1}$. The BJH calculation performed to evaluate pore volume and pore size distribution of nanoparticles. The results showed that the pore volume and the pore size of MMNP/BQ-E were 0.1318 $cm^3\,g^{-1}$ and 18.713 nm, respectively.

3.2. Optimization studies

3.2.1. Effect of pH

To investigate the optimum pH in the adsorption process, the experiments were performed within different ranges of pH (3–10). Fig. 7 shows that pH affects the surface charge of adsorbent, and the speciation of the adsorbate during
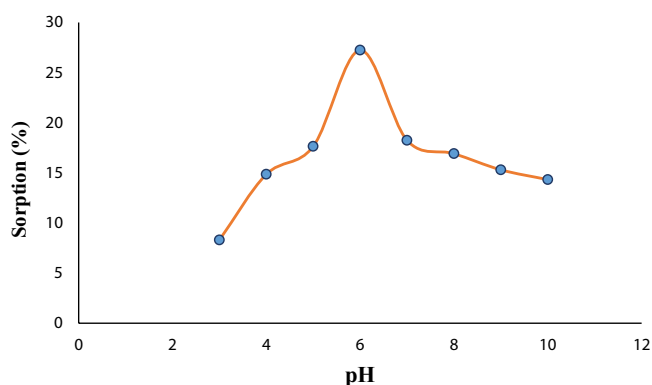
Fig. 7. Effect of pH on HA adsorption; sorbent weight 2 mg, contact time 5 min, initial concentration 20 mg L^{-1} at 25°C.

the reaction. Therefore, determination of optimum pH is very important for the adsorption process [20]. At acidic pH, with conversion of the hydroxyl group (OH) to OH^{+2}, the hydrogen bond is reduced, which leads to adsorption of a diminished amount of HA. It is believed that at neutral pH (6–7), the concentration of H^{+} drops; thus, the hydrogen bond increases. Also, the electrostatic attraction between carboxylic groups of HA and amino group MMNP/BQ-E was strongest, thereby enhancing the adsorption. At pH values higher than 7, due to ionization of hydroxyl groups to O^{-}, the adsorption capacity of HA on MMNP/BQ-E has decreased. The pH levels exceeding 10 were not investigated since the nano-sorbent is not dissolved at alkaline pHs. Based on Fig. 7, the optimum pH was found at pH = 6.

3.2.2. Effect of contact time

In order to investigate the effect of the contact time on the removal of HA by MMNP/BQ-E, experiments were performed at different contact times, with 11 solutions which each solution stirred in a specific period of time (5–120 min; Fig. 8). The contact time curves indicated that the adsorption of HA occurred quickly up to 15 min, suggesting that there were many available adsorption sites on the MMNP/BQ-E. Thereafter, however, due to the saturation of the binding sites and achieving equilibrium, the adsorption rate diminished [22]. Finally, 20 min was chosen as the optimum contact time for HA adsorption.
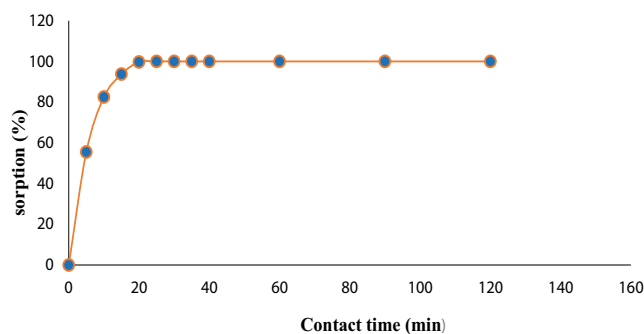

Fig. 8. Effect of contact time on HA adsorption; sorbent weight 2 mg, pH = 6, initial concentration 20 mg L^{-1} at 25°C.

3.2.3. Effect of initial concentration

As presented in Fig. 9, when the initial concentration was elevated from 1 to 10 mg/mg L^{-1}, the extent of removal percentage grew by approximately 80%. In the process of removal, the absorption rate declined sharply for concentrations beyond 10 mg L^{-1}. According to previous studies, at low concentrations of HA, all adsorbent ions in the adsorption medium can communicate with the binding sites leading to increased absorption. In contrast, at higher concentrations of HA, the access to the adsorption sites diminishes, thus compromising the adsorption process [14].

3.2.4. Effect of adsorbent dosage

The effect of adsorbent dosage was investigated by six different amounts (0.05–1 g) of MMNP/BQ-E, with the results shown in Fig. 10. By increasing the sorbent value from 0.05 to 0.5, the removal of HA has increased, which is attributed to many available adsorption sites [35]. After reaching the maximum removal percentage at 0.5 g, no significant change was observed with increasing amounts. Therefore, 0.5 g of adsorbent under experiment conditions offered adequate adsorption sites to achieve 99% removal.

3.3. Adsorption kinetics

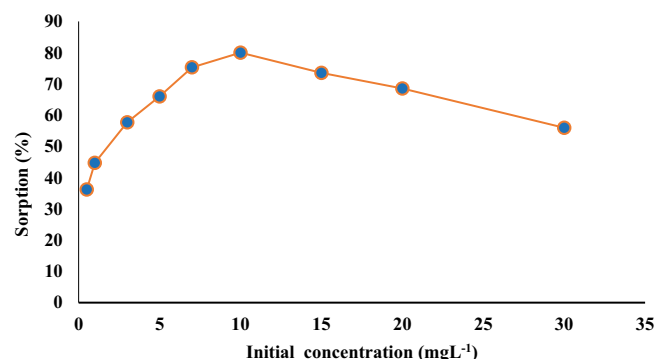To investigate the kinetic mechanism of the HA adsorption process on MMNP/ BQ-E, the pseudo-first-order [5]

Fig. 9. Effect of initial concentration on HA adsorption (1–30 mg L^{-1}); sorbent weight 2 mg, pH = 6, contact time 20 min at 25°C.

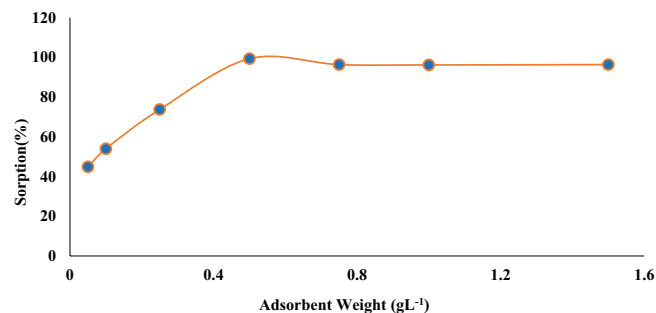Fig. 10. Effect of adsorbent weight on HA adsorption and distribution coefficient; pH = 6, contact time 20 min, initial concentration 10 mg L^{-1} at 25°C.

and pseudo-second-order rate [36] models were applied for experimental data (Figs. 11 and 12). The adsorption amount for MMNP/BQ-E was specified at different contact times (5–120 min) under optimal pH with the sorbent weight optimized at 25°C. The pseudo-first and second-order model are presented by Eqs. (5) and (6), respectively [37]:

$$q_t = q_e \left(1 - e^{-k_1 t}\right) \tag{5}$$

$$q_t = \frac{t q_e^2}{1/k_2^2 + q_e t} \tag{6}$$

where q_e (mg g^{-1}) is the extent of HA adsorption at equilibrium, q_t (mg g^{-1}) is the magnitude of HA adsorption at a specific time (min), k_1 (min^{-1}) is the Lagergren rate constant of the equation, and k_2 (g mg^{-1} min^{-1}) shows the rate constant of adsorption of pseudo-second-order model. Regarding the regression coefficient (R^2) for kinetic models, it was assumed that the HA adsorption process occurs as chemical removal controlled by the pseudo-second-order model [38] (Table 1).
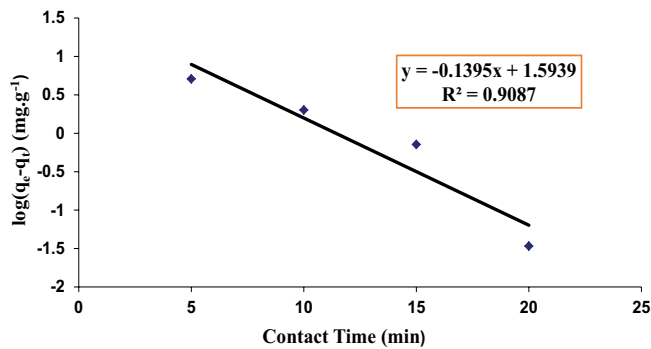

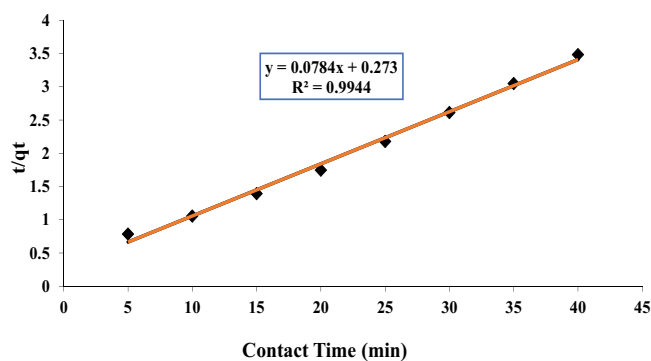Fig. 11. Pseudo-first-order plots of HA onto MMNP/BQ-E.

Fig. 12. Pseudo-second-order plots of HA onto MMNP/BQ-E.

3.4. Adsorption isotherms

To investigate the adsorption capacity and MMNP/BQ-E adsorption behavior, five common isotherms models, Langmuir; Freundlich; Temkin; Redlich–Peterson; and Dubinin–Radushkevich (D–R), were used (Figs. (13)–(17)). The linearized form of the Langmuir equation which is used for monolayer adsorption is described by Eq. (7) [39–41].

$$\frac{C_e}{q_e} = \frac{1}{K_L q_m} + \frac{C_e}{q_m} \tag{7}$$

where q_m is the maximum monolayer adsorption capacity (mg g^{-1}), K_L is the Langmuir constant related to the free energy of adsorption (L mg^{-1}), and a plot of C_e/q_e vs. C_e yields a straight line with slope $1/q_m$ and intercept $1/q_m K_L$. The well-known form of the Freundlich isotherm is given by Eq. (8):

$$q_e = K_f C_e^{\frac{1}{n}} \tag{8}$$

Fig. 13. Langmuir isotherms model to adsorption HA on MMNP/BQ-E.
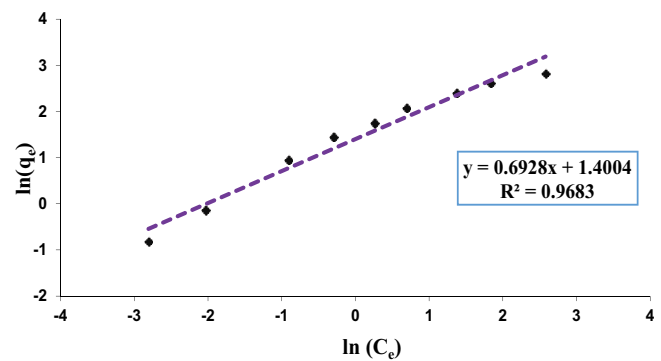
Fig. 14. Freundlich isotherm model to adsorption HA on MMNP/BQ-E.

Table 1
Parameters of pseudo-first and second-order

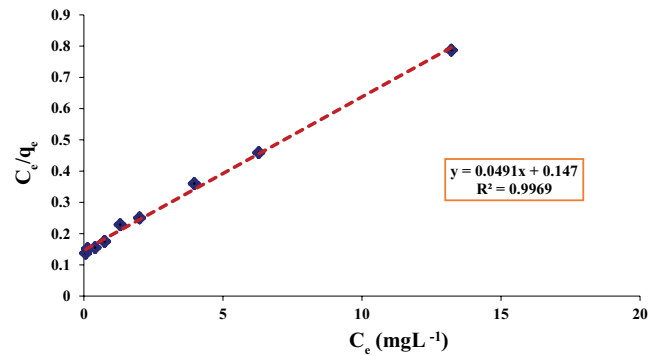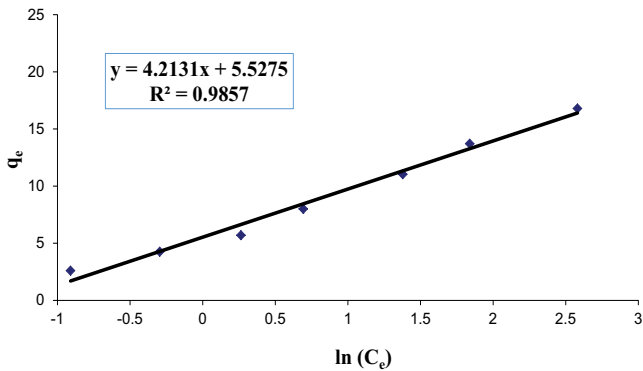| Kinetic model	Equation	q_e (mg g^{-1})	k_1 (min^{-1})	R^2
Pseudo-first-order	$-0.1395x + 1.5939$	39.25	0.313	0.90
Pseudo-second-order	$0.0784x + 0.273$	12.75	0.022	0.99

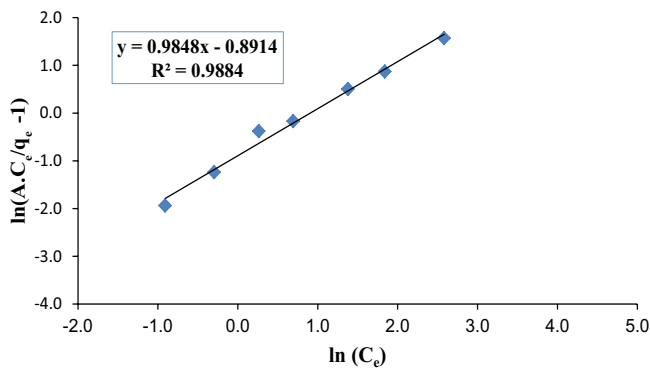Fig. 15. Temkin Isotherm model to adsorption HA on MMNP/BQ-E.

Fig. 16. Redich Peterson isotherm model to adsorption HA on MMNP/BQ-E.
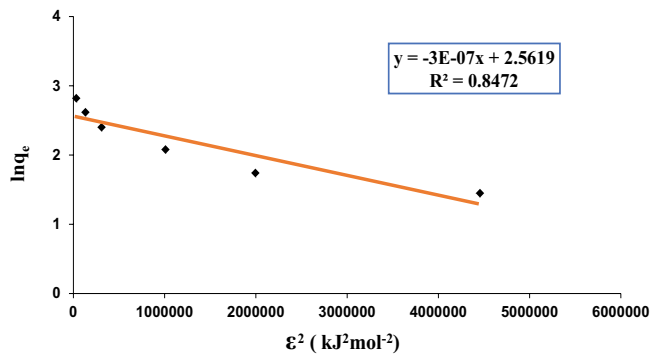

Fig. 17. D–R isotherm model to adsorption HA on MMNP/BQ-E.

which after applying logarithm for both sides, converted into Eq. (9) as follows:

$$\log\left(q_e\right) = \log\left(K_f\right) + \frac{1}{n}\log\left(C_e\right) \tag{9}$$

where K_f and $1/n$ are the Freundlich constants related to the adsorption capacity and adsorption intensity, respectively.

The next popular isotherm model is D–R for which the non-linear form is given by Eq. (10) [42]:

$$q_e = q_{max}e^{-K_{ad}\varepsilon^2} \tag{10}$$

The linear form can be represented by Eq. (11):

$$\ln\left(q_e\right) = \ln\left(q_{max} - K_{ad}\varepsilon^2\right) \tag{11}$$

where q_e is the amount of HA (mmol g⁻¹) adsorbed per unit mass of MMNP/BQ-E, q_{max} is the theoretical adsorption capacity (mmol g⁻¹), K_{ad} is the constant related to the adsorption energy (mol² kJ⁻²), and ε is the Polanyi potential that is determined as Eq. (12):

$$\varepsilon = RT\ln\left(1 + \frac{1}{C_e}\right) \tag{12}$$

where C_e is the solution concentration at equilibrium (mol L⁻¹), R is the gas constant (8.314 J mol⁻¹ K⁻¹), and T is the absolute temperature of the aqueous solution (K). The amount of K_{ad} was estimated from the slope of the plot of ln q_e vs. ε^2 and q_{max} is prepared from the intercept. As stated, K_{ad} is related to adsorption energy, so the mean free energy of adsorption (E; kJ mol⁻¹) is calculated according to Eq. (13) as follows:

$$E = \frac{1}{\sqrt{2K_{ad}}} \tag{13}$$

Another popular isotherm model is Temkin. In this model, some interactions occur between adsorbent and adsorbate which cause a linear decrease in the heat of adsorption (Eq. (14)) [43,44].

$$q_e = B\ln C_e + B\ln A \tag{14}$$

In this equation, $B = RT/b$ and b (J mol⁻¹) is related to the heat of adsorption, R (8.314 Jmol⁻¹K⁻¹) is the universal gas constant, A (L mg⁻¹) is Temkin model constant, and T is absolute temperature (K) [45].

Redlich–Peterson model can explain combinational homogeneous and heterogeneous adsorption systems. This model presentation Langmuir and Freundlich isotherm properties in one equation Eq. (15) [44]:

$$\left(\frac{C_e}{q_e} - 1\right) = g\ln C_e + \ln B \tag{15}$$

In Eq. (15), A and B are Redlich–Peterson parameters. Also, the g value ($0 < g \le 1$) is dimensionless. Estimated constants for this isotherm can be reached by plotting linear diagram of ln[$A(C_e/q_e) - 1$] vs. ln (C_e). In this model, $g \approx 1$ confirms Langmuir model whereas $g \approx 0$ approves Freundlich model [46].

The Redlich–Peterson isotherm model and other parameters confirmed that the Langmuir model is the dominant isotherm for this study. During the absorption mechanism, the OH bond of HA makes hydrogen bonding in the form of monolayers homogenous with amine groups on the sorbent surface [46]. The adsorption isotherm was surveyed at the initial concentration of HA (1–30 mg L⁻¹) under optimal conditions with pH = 6 at 25°C. Regarding Table 2, the regression coefficient indicates that the Langmuir model was more suitable for the adsorption process (Fig. 13).

Table 2
Equilibrium isotherm parameters of sorption of HA

Isotherms		
Langmuir	Equation:	$0.0491x + 0.147$
	q_m (mg g^{-1})	20.36
	k_L (L mg^{-1})	0.3340
	R_L	0.0907
	R^2	0.9969
Freundlich	Equation:	$0.6928x + 1.4004$
	K_f (mg g^{-1})	4.05
	n (g L^{-1})	1.44
	R^2	0.9683
Temkin	Equation:	$4.2131x + 5.5275$
	b (J mol^{-1})	588.3599
	A (L mg^{-1})	3.713517
	R^2	0.9857
Redlich–Peterson	Equation:	$0.9848x$-0.8914
	R^2	0.9884
Dubinin–Radushkevich (D–R)	Equation:	$-3E-07x + 2.5619$
	K_{ad} (mol^2 kJ^{-2})	0.0000003
	q_{max} (mmol g^{-1})	12.96
	R^2	0.8472

Accordingly, the adsorption reaction occurred as monolayer adsorption [47] on the MMNP/BQ-E surface. The maximum adsorption capacity for HA was 20.36 mg g^{-1}, indicating a great potential for HA removal from aquatic solutions. The maximum adsorption capacity for HA optioned from this study has been compared with that of some other adsorbents in Table 3.

3.5. Reusability of MMNP/BQ-E

In order to estimate the reusability of MMNP/BQ-E adsorbent, the adsorption–desorption cycle repeated eight times under optimal conditions (pH = 6, adsorbent dosage = 0.5 g L^{-1}, and contact time 20 min; Table 4). After each adsorption cycle, the adsorbent conducted with 0.01 M NaOH in 10 mL ethanol solution. The same adsorbent was used for all the eight cycles of the adsorption–desorption mechanism.

Table 4
Desorption results (%) in 0.01 M NaOH in 10 mL methanol solution on MMNP/BQ-E loaded with HA

Cycle	Adsorption capacity (%)
1	99.51
2	96.38
3	94.8
4	84.50
5	78.71
6	72.3
7	68.28
8	64

The adsorption capacity for first to third cycles was 99.51%, 96.38%, and 94.80%, respectively, which shows high adsorption rate of HA. The removal efficiency of HA decreased continuously from the first to the last cycles and reached 64% in the eighth cycle. This reduction efficiency of HA adsorption could have been occurred due to the decrease of available actives sites at the surface of the sorbent. Based on the high efficiency of HA removal by MMNP/BQ-E adsorbent, the procedure is cost-effective from economical point of view [50].

3.6. Effective of ionic strength on the HA adsorption onto MMNP/BQ-E

Results showed that by increasing the ionic strength, the HA adsorption decreases. The reduction efficiency of HA adsorption in high ionic strength solution could be related to decreasing the interactions because of covering the surface of sorbent by NaCl (Fig. 18) [48].

3.7. Thermodynamic studies

To evaluate how the adsorption process has occurred in nature, we used thermodynamic studies. For this purpose, the results obtained from different temperatures were used to calculate the thermodynamic parameters. Based on changes in the equilibrium constants with temperature, one can consider the enthalpy change ($\Delta H°$), Gibbs free energy change ($\Delta G°$), and entropy change ($\Delta S°$). The distribution coefficient could be related to the enthalpy and entropy

Table 3
Compared maximum adsorption capacity (mg g^{-1}) of HA from this study (sorption condition: the initial concentration of HA [1–30 mg L^{-1}] under optimal conditions with pH = 6 at 25°C) to some other adsorbents [5,25,47–49]

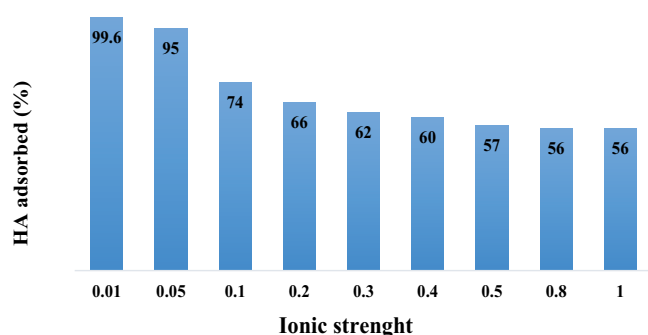| No.	Adsorbent	q_m (mg g^{-1})	Pollutant	Reference
1	Aminopropyl functionalized rice husk ash	8.2	HA	[25]
2	Cetylpyridinium bromide	92	HA	[5]
3	Mg/Fe layered double hydroxide	25.6	HA	[48]
4	NiFe$_2$O$_4$ nanoparticles	5.2	HA	[47]
5	Fe$_3$O$_4$-chitosan hybrid nano-particles	44.84	HA	[49]
6	MMNP/BQ-E	20.36	HA	This study

Fig. 18. Effect of ionic strength on the HA adsorption onto MMNP/BQ-E.

change at a constant temperature (T^{-1}) by rearranging the Van't Hoff equation (Eq. (16)):

$$\ln\left(K_d\right) = \frac{\Delta S^{\circ}}{R} - \frac{\Delta H^{\circ}}{RT} \qquad (16)$$

where $\ln(K_d)$ is the distribution coefficient (mL g^{-1}); (ΔS°) shows standard entropy; (ΔH°) represents standard enthalpy; T denotes the absolute temperature (K); and R reflects the gas constant (kJ mol^{-1} K^{-1}).

The standard free energy value is calculated by Eq. (17):

$$\Delta G^{\circ} = \Delta H^{\circ} - T\Delta S^{\circ} \qquad (17)$$

The experiments were performed using a solution concentration of 100 mg L^{-1} of HA at five temperatures (25°C, 30°C, 35°C, 40°C, and 45°C) (Fig. 19).

The values of ΔH° and ΔS° were calculated from the slopes and intercepts of a linear regression of $\ln (K_d)$ vs. T^{-1} ($R^2 > 0.97$). The results revealed that the adsorption capacity of the MMNP/BQ-E increased with temperature rise and the adsorption process was endothermic (Table 5).

At all different temperatures, the values of Gibbs free energy (ΔG°) were negative suggesting the spontaneity of the removal process. The positive value of ($\Delta S^{\circ} > 0$) indicated that greater randomness has increased during the adsorption of HA on MMNP/BQ-E in the system and revealed high stability of adsorption [51]. The positive ΔH° values showed
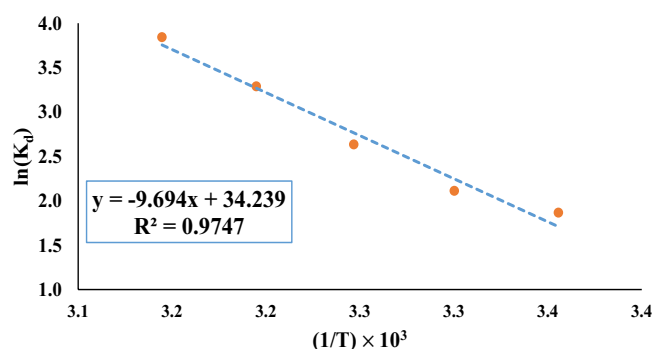
Table 5
Thermodynamic parameters for adsorption of HA onto MMNP/BQ-E

Adsorbent	Temperature (K)	ΔG° (kJ mol^{-1})	ΔH° (kJ mol^{-1})	ΔS° (kJ K^{-1} mol^{-1})
MMNP/ BQ-E	298	−84.6	80.4602	284.1837
	303	−86.0		
	308	−87.4		
	313	−88.9		
	318	−90.3		

that the HA adsorption process is endothermic in nature, where with elevation of temperature, the adsorption of HA on MMNP/BQ-E has grown [13].

4. Conclusion

In this study, novel core-shell structured nanoparticles were synthesized. The characterization of MMNP/BQ-E was accomplished via FTIR, XRD, XPS, SEM, EDX, BJH, and BET. The specific surface area of MMNP/BQ-E was found to be 58.34 m^{2}g^{-1}. The characterization results confirmed that MMNP/BQ-E was successfully coated onto the surface of Fe$_3$O$_4$. The crystalline size of the nanoparticles obtained from XRD was about 11.26 nm. For the pH, contact time, the adsorbent weight, and the initial concentration of HA, the optimal values obtained were 6, 20 min, 0.5 g L^{-1}, 10 mg L^{-1}, respectively. The adsorption isotherm indicated the highest correlation with the Langmuir model ($R^2 = 99$%) with an adsorption capacity of 20.36 mg g^{-1}. Investigation of adsorption kinetics showed that adsorption of HA on MMNP/BQ-E can be a chemical reaction controlled by pseudo-second-order kinetic model. Having examined the thermodynamic parameters, it was found that the reaction was spontaneous and endothermic under laboratory conditions, with the values of enthalpy change (ΔH°) and entropy change (ΔS°) obtained as 80.4602 kJ mol^{-1} and 284.1837 kJ K^{-1} mol^{-1}, respectively.

Fig. 19. Temperature dependence of the adsorption of HA for MMNP/BQ-E.

References

[1] F.J. Stevenson, Humus Chemistry: Genesis, Composition, Reactions, John Wiley & Sons, 1994.
[2] E. Loffredo, N. Senesi, The Role of Humic Substances in the Fate of Anthropogenic Organic Pollutants in Soil With Emphasis on Endocrine Disruptor Compounds, In: Soil and Water Pollution Monitoring, Protection and Remediation, Springer, Dordrecht, 2006, pp. 69–92.
[3] A. Schafer, Natural Organics Removal Using Membranes: Principles, Performance, and Cost, CRC Press, 2001.
[4] S. Assemi, P.G. Hartley, P.J. Scales, R. Beckett, Investigation of adsorbed humic substances using atomic force microscopy, Colloids Surf., A, 248 (2004) 17–23.
[5] Y. Zhan, Z. Zhu, J. Lin, Y. Qiu, J. Zhao, Removal of humic acid from aqueous solution by cetylpyridinium bromide modified zeolite, J. Environ. Sci., 22 (2010) 1327–1334.
[6] H. Gallard, U. von Gunten, Chlorination of natural organic matter: kinetics of chlorination and of THM formation, Water Res., 36 (2002) 65–74.

[7] T. Hartono, S. Wang, Q. Ma, Z. Zhu, Layer structured graphite oxide as a novel adsorbent for humic acid removal from aqueous solution, J. Colloid Interface Sci., 333 (2009) 114–119.

[8] S. Wang, Q. Ma, Z.H. Zhu, Characteristics of coal fly ash and adsorption application, Fuel, 87 (2008) 3469–3473.

[9] C.S. André, M. Khraisheh, Removal of humic substances from drinking water using GAC and iron-coated adsorbents: consideration of two kinetic models and the influence of mixing, Environ. Eng. Sci., 26 (2009) 235–244.

[10] A. Norfazliana, A.R. Mukhlis, O. Mohd Hafiz Dzarfan, J. Juhana, A.A. Azian, Preparation, characterizations and performance evaluations of alumina hollow fiber membrane incorporated with UiO-66 particles for humic acid removal, J. Membr. Sci., 563 (2018) 162–174.

[11] E. Derakhshani, A. Naghizadeh, Optimization of humic acid removal by adsorption onto bentonite and montmorillonite nanoparticles, J. Mol. Liq., 259 (2018) 76–81.

[12] J.S. Salla, N. Padoin, S.M. Amorim, G. Li Puma, R.F.P.M. Moreira, Humic acids adsorption and decomposition on Mn_2O_3 and α-Al_2O_3 nanoparticles in aqueous suspensions in the presence of ozone, J. Environ. Chem. Eng., (2018), doi.org/10.1016/j.jece.2018.11.025.

[13] T. Ye, W. Chen, H. Xu, N. Geng, Y. Cai, Preparation of TiO_2/graphene composite with appropriate N-doping ratio for humic acid removal, J. Mater. Sci., 53 (2018) 613–625.

[14] Y. Yan, G. Yuvaraja, C. Liu, L. Kong, K. Guo, G.M. Reddy, G.V. Zyryanov, Removal of Pb(II) ions from aqueous media using epichlorohydrin crosslinked chitosan Schiff's base@ Fe_3O_4 ($ECCSB@Fe_3O_4$), Int. J. Biol. Macromol., 117 (2018) 1305–1313.

[15] B. Rouhi Broujeni, A. Nilchi, A.H. Hassani, R. Saberi, Preparation and characterization of chitosan/Fe_2O_3 nano composite for the adsorption of thorium (IV) ion from aqueous solution, Water Sci. Technol., 78 (2018) 708–720.

[16] H. Lu, J. Wang, F. Li, X. Huang, B. Tian, H. Hao, Highly efficient and reusable montmorillonite/Fe_3O_4/humic acid nano-composites for simultaneous removal of Cr(VI) and aniline, Nanomaterials, 8 (2018) 537.

[17] T.D. Minh, B.K. Lee, M.T. Nguyen-Le, Methanol-dispersed of ternary $Fe_3O_4@\gamma$-APS/graphene oxide-based nanohybrid for novel removal of benzotriazole from aqueous solution, J. Environ. Manage., 209 (2018) 452–461.

[18] S. Hashemipour, H.A. Panahi, Fabrication of magnetite nanoparticles modified with copper based metal organic framework for drug delivery system of letrozole, J. Mol. Liq., 243 (2017) 102–107.

[19] A.W. Burton, K. Ong, T. Rea, I.Y. Chan, On the estimation of average crystallite size of zeolites from the Scherrer equation: a critical evaluation of its application to zeolites with one-dimensional pore systems, Microporous Mesoporous Mater., 117 (2009) 75–90.

[20] G. Huang, H. Zhang, J.X. Shi, T.A.G. Langrish, Adsorption of chromium(VI) from aqueous solutions using cross-linked magnetic chitosan beads, Ind. Eng. Chem. Res., 48 (2009) 2646–2651.

[21] F. Arias, T.K. Sen, Removal of zinc metal ion (Zn^{2+}) from its aqueous solution by kaolin clay mineral: a kinetic and equilibrium study, Colloids Surf., A, 348 (2009) 100–108.

[22] M. Ahmaruzzaman, V.K. Gupta, Rice husk and its ash as low-cost adsorbents in water and wastewater treatment, Ind. Eng. Chem. Res., 50 (2011) 13589–13613.

[23] Y. Ren, X. Wei, M. Zhang, Adsorption character for removal Cu(II) by magnetic Cu(II) ion imprinted composite adsorbent, J. Hazard. Mater., 158 (2008) 14–22.

[24] B.R. Broujeni, A. Nilchi, Preparation and characterization of polyacrylonitrile/aluminum oxide nanofiber adsorbent modified with 2-amino-3-methyl-1-hexanethiol for the adsorption of Thorium (IV) ion from aqueous solution, J. Environ. Eng., 144 (2018) 04018099-1–04018099-11.

[25] A. Imyim, E. Prapalimrungsi, Humic acids removal from water by aminopropyl functionalized rice husk ash, J. Hazard. Mater., 184 (2010) 775–781.

[26] U. Kurtan, A. Baykal, Fabrication and characterization of $Fe_3O_4@$APTES@PAMAM-Ag highly active and recyclable magnetic nanocatalyst: catalytic reduction of 4-nitrophenol, Mater. Res. Bull., 60 (2014) 79–87.

[27] P. Misaelides, Application of Particle and Laser Beams in Materials Technology, Springer, Dordrecht, 2013, 283 p.

[28] M. Khalkhali, S. Sadighian, K. Rostamizadeh, F. Khoeini, M. Naghibi, N. Bayat, M. Habibizadeh, M. Hamidi, Synthesis and characterization of dextran coated magnetite nanoparticles for diagnostics and therapy, Bioimpacts, 5 (2015) 141.

[29] B.-f. Pan, F. Gao, H.-c. Gu, Dendrimer modified magnetite nanoparticles for protein immobilization, J. Colloid Interface Sci., 284 (2005) 1–6.

[30] N. Parham, H.A. Panahi, A. Feizbakhsh, E. Moniri, Synthesis of high generation thermo-sensitive dendrimers for extraction of rivaroxaban from human fluid and pharmaceutic samples, J. Chromatogr. A, 1545 (2018) 12–21.

[31] N. Kemikli, H. Kavas, S. Kazan, A. Baykal, R. Ozturk, Synthesis of protoporphyrin coated superparamagnetic iron oxide nanoparticles via dopamine anchor, J. Alloys Compd., 502 (2010) 439–444.

[32] Y. Wang, P. Su, S. Wang, J. Wu, J. Huang, Y. Yang, Dendrimer modified magnetic nanoparticles for immobilized BSA: a novel chiral magnetic nano-selector for direct separation of racemates, J. Mater. Chem., 1 (2013) 5028–5035.

[33] Y. Jiang, J. Jiang, Q. Gao, M. Ruan, H. Yu, L. Qi, A novel nanoscale catalyst system composed of nanosized Pd catalysts immobilized on $Fe_3O_4@SiO_2$–PAMAM, Nanotechnology, 19 (2008) 075714.

[34] S. Lian, Z. Kang, E. Wang, M. Jiang, C. Hu, L. Xu, Convenient synthesis of single crystalline magnetic Fe_3O_4 nanorods, Solid State Commun., 127 (2003) 605–608.

[35] L. Wang, J. Zhang, R. Zhao, C. Li, Y. Li, C. Zhang, Adsorption of basic dyes on activated carbon prepared from Polygonum orientale Linn: equilibrium, kinetic and thermodynamic studies, Desalination, 254 (2010) 68–74.

[36] J. Fan, W. Cai, J. Yu, Adsorption of N719 dye on anatase TiO_2 nanoparticles and nanosheets with exposed (001) facets: equilibrium, kinetic, and thermodynamic studies, Chem. Asian J., 6 (2011) 2481–2490.

[37] B.R. Broujeni, A. Nilchi, A.H. Hassani, R. Saberi, Application of chitosan/Al_2O_3 nano composite for the adsorption of thorium (IV) ion from aqueous solution, Desal. Wat. Treat., 106 (2018) 125–133.

[38] J.-P. Fan, X.-K. Xu, R. Xu, X.-H. Zhang, J.-H. Zhu, Preparation and characterization of molecular imprinted polymer functionalized with core/shell magnetic particles ($Fe_3O_4@SiO_2@$MIP) for the simultaneous recognition and enrichment of four taxoids in Taxus × media, Chem. Eng. J., 279 (2015) 567–577.

[39] N.K. Amin, Removal of direct blue-106 dye from aqueous solution using new activated carbons developed from pomegranate peel: adsorption equilibrium and kinetics, J. Hazard. Mater., 165 (2009) 52–62.

[40] H. Cherifi, S. Hanini, F. Bentahar, Adsorption of phenol from wastewater using vegetal cords as a new adsorbent, Desalination, 244 (2009) 177–187.

[41] I. Langmuir, The constitution and fundamental properties of solids and liquids. Part I. Solids, J. Am. Chem. Soc., 38 (1916) 2221–2295.

[42] E. Metwally, T. El-Zakla, R.R. Ayoub, Thermodynamics study for the sorption of ^{134}Cs and ^{60}Co radionuclides from aqueous solutions, J. Nucl. Radiochem. Sci., 9 (2008) 1–6.

[43] M.J. Temkin, V. Pyzhev, Recent modifications to Langmuir isotherms, Acta Physiochim URSS, 12 (1940) 217–225.

[44] C.B. Vidal, A.L. Barros, C.P. Moura, A.C.A. de Lima, F.S. Dias, L.C.G. Vasconcellos, P.B.A. Fechine, R.F. Nascimento, Adsorption of polycyclic aromatic hydrocarbons from aqueous solutions by modified periodic mesoporous organosilica, J. Colloid Interface Sci., 357 (2011) 466–473.

[45] A. Torabian, H.A. Panahi, G.R. Nabi Bid Hendi, N. Mehrdadi, Synthesis, modification and graft polymerization of magnetic nano particles for PAH removal in contaminated water, J. Environ. Health Sci. Eng., 12 (2014) 105.

[46] M. Belhachemi, F. Addoun, Comparative adsorption isotherms and modeling of methylene blue onto activated carbons, Appl. Water Sci., 1 (2011) 111–117.

[47] S.V. Bhosale, D.N. Bankar, S.V. Bhoraskar, V.L. Mathe, Analysis of electrokinetic properties of $NiFe_2O_4$ nanoparticles synthesized by DC thermal plasma route and its use in adsorption of humic substances, J. Environ. Chem. Eng., 4 (2016) 1584–1593.

[48] M.S. Gasser, H.T. Mohsen, H.F. Aly, Humic acid adsorption onto Mg/Fe layered double hydroxide, Colloids Surf., A, 331 (2008) 195–201.

[49] M.A. Zulfikar, S. Afrita, D. Wahyuningrum, M. Ledyastuti, Preparation of Fe_3O_4-chitosan hybrid nano-particles used for humic acid adsorption, Environ. Nanotechnol. Monit. Manage., 6 (2016) 64–75.

[50] Z. Qi, T.P. Joshi, R. Liu, H. Liu, J. Qu, Synthesis of Ce(III)-doped Fe_3O_4 magnetic particles for efficient removal of antimony from aqueous solution, J. Hazard. Mater., 329 (2017) 193–204.

[51] M.A. Zulfikar, I. Afrianingsih, A. Bahri, M. Nasir, A. Alni, H. Setiyanto, Removal of humic acid from aqueous solution using dual PMMA/PVDF composite nanofiber: kinetics study, J. Phys. Conf. Ser., 1013 (2018), Article ID: 012202.